1 **Wall teichoic acids regulate peptidoglycan synthesis by paving cell wall nanostructure**

2 Felix Barber[1], Zarina Akbary[1], Zhe Yuan[1], Jacob Biboy[2], Waldemar Vollmer[3], Enrique R. Rojas[1,*]

3 1: Center for Genomics and Systems Biology, New York University, New York 10003, United States.

4 2: Center for Bacterial Cell Biology, Newcastle University, Newcastle upon Tyne NE2 4AX, United

5 Kingdom.

6 3: Institute for Molecular Bioscience, The University of Queensland, Brisbane, Australia.

7

8 *Correspondence: rojas@nyu.edu

9

10 **Keywords:** Rod complex, bacterial growth, cell shape, morphogenesis, *Bacillus subtilis*

Summary

The bacterial cell wall is a polymeric exoskeleton, composed largely of peptidoglycan, that determines cell size and shape. Two systems synthesize peptidoglycan during the growth of rod-shaped bacteria, which are found pervasively across diverse bacterial taxa: the multi-protein Rod complexes are critical for cell shape because they synthesize anisotropic peptidoglycan oriented along the cell circumference[1–3], whereas PBP1 synthesizes isotropic peptidoglycan[1,4] (Fig. 1A). In Gram-positive bacteria, rod shape is also dependent on wall teichoic acids[5], an abundant cell wall polymer, for entirely unknown reasons. Here, we show that teichoic acids occlude nanoscopic pores in the cell wall, which simultaneously promotes Rod complex activity and inhibits PBP1. Depletion of teichoic acids exposed these pores within minutes, coinciding with a rapid activation of PBP1. In contrast to previous steady-state measurements[6,7], we found that teichoic acid depletion also caused the transient arrest of Rod complexes prior to the onset of amorphous growth. Teichoic acids, therefore, are a new critical factor in peptidoglycan synthesis regulation. Our work further identifies the cell wall, via its molecular-scale structure, as a non-canonical auto-regulatory factor in its own synthesis. Since teichoic acids additionally govern peptidoglycan hydrolysis[8–13], our results position these polymers as "master regulators" of rod-shaped cell growth.

27 **Introduction**

28 The bacterial cell wall is a solid polymeric macromolecule that protects cells from lysis in many contexts,
29 including pathogenesis[14] and antibiotic treatment[15]. Furthermore, the cell wall precisely determines cell
30 shape (Fig. 1A), which affects many aspects of cellular physiology[3,16,17] — the most pervasive shape
31 across bacteria is the bacillus, or "rod"[18]. The cell wall consists primarily of peptidoglycan: glycan
32 polymers that are crosslinked by short peptides. In Gram-positive bacteria, peptidoglycan is covalently
33 modified with wall teichoic acids, negatively charged polymers of sugar alcohol-phosphate subunits
34 (hereafter "teichoic acids," distinct from the membrane-anchored lipoteichoic acids)[19,20]. Teichoic acids
35 are typically nonessential[5,21], however, inhibiting their synthesis causes *Bacillus subtilis* and the serious
36 pathogen *Listeria monocytogenes* to grow amorphously and slowly[5,21]. How teichoic acids enable rod-
37 shaped morphogenesis is unknown[5,21,22].

38

39 Homeostasis of rod shape is thought to be governed by the two primary molecular mechanisms of
40 peptidoglycan synthesis. First, the essential, multi-protein Rod complexes synthesize anisotropic
41 peptidoglycan that structurally reinforces the cell wall along its circumference (Fig. 1A), providing the
42 mechanical basis for rod shape[1,2]. Anisotropic peptidoglycan synthesis results from the circumferential
43 motion of Rod complexes along the plasma membrane[23–25]. In *B. subtilis*, this motion is oriented by actin
44 homologs MreB, Mbl and MreBH[26,27,6], and is driven by peptidoglycan synthesis itself[23]. Circumferential
45 motion, therefore, is a direct indicator for Rod complex activity[28,29]. Within the Rod complex,
46 peptidoglycan polymerization is catalyzed by the transglycosylase RodA[30] (drawing from lipid II
47 precursors in the plasma membrane), while cross-linking to acceptor peptides within the cell wall is
48 catalyzed by the transpeptidases PBP2A and PBPH[4,31] ("Class B" PBPs).

49

50 By contrast to the Rod complexes, the non-essential enzyme PBP1 is a large, multi-domain protein (a
51 "Class A" PBP, encoded by *ponA*[32]) that synthesizes isotropic peptidoglycan (Fig. 1A). It is thought to
52 specifically repair pores in the cell wall that arise during the rapid cell-wall turnover required for cell
53 growth[4,33]. Because Rod complexes synthesize peptidoglycan anisotropically and PBP1 synthesizes it
54 isotropically, the balance of their expression determines cell width[1], and strong overexpression of PBP1
55 causes semi-amorphous growth.

56

57 Teichoic acids influence diverse cellular phenotypes including antimicrobial resistance[34,35], protein
58 localization within the cell envelope[36], pathogenesis[37], cation homeostasis[38,39] and autolysis[8–11]. It is
59 unclear, however, how these processes would account for teichoic acids' influence on cell shape
60 according to the Rod complex-PBP1 model. One possibility is that Rod complexes are directly,
61 biochemically activated by teichoic acids[40]. This model is consistent with the observations that teichoic
62 acid synthases and peptidoglycan synthesis machinery both exhibit punctate spatial patterning[41], and
63 that the syntheses of the two materials are co-local in both *B. subtilis*[42] and *Streptococcus pneumoniae*[43].
64 However, teichoic acid synthases do not exhibit the circumferential motion characteristic of Rod
65 complexes, and Rod complexes still translocate along the cell membrane in amorphous cells depleted
66 for TagO, the enzyme that catalyzes the first committed reaction of teichoic acid synthesis[6,7]. Given
67 these conflicting data, there is no known mechanistic interaction(s) between teichoic acids and either of
68 the two peptidoglycan biosynthesis pathways.

69

70

71

72 **Results**

73 **Inhibiting wall teichoic acid synthesis reduces growth rate prior to cell shape loss**

74 *Bacillus subtilis* mutants that lack teichoic acids (Δ*tagO*) grow amorphously and slowly in bulk liquid
75 culture (≈4 times slower than wild-type, rod-shaped cells)[5]. To interrogate this dependence, we first
76 measured the dynamics of growth rate and cell shape upon teichoic acid depletion. We used a
77 microfluidic perfusion chamber to acutely treat exponentially growing, wild-type *B. subtilis* cells with
78 tunicamycin, which specifically inhibits TagO at low concentrations[35,44–46] (Fig. S1A,B) and then
79 computed the single-cell growth rate and width from timelapse micrographs. Approximately 10 minutes
80 after tunicamycin treatment, growth rate decreased from its steady-state value in rich medium (LB),
81 plateaued temporarily, and then decreased a second time until it reached its steady-state value in
82 tunicamycin (Fig. 1B). Cells retained their untreated rod shape until the second decrease in elongation
83 rate when they began to widen, eventually losing rod shape altogether (Fig. S2A). Amorphous cells
84 continued to grow indefinitely (Video S1). We also observed a decrease in the single-cell growth rate
85 prior to the loss of cell shape when we acutely inhibited *tagO* transcription (Fig. S2B,C).

86

87 **Inhibiting wall teichoic acid synthesis reduces Rod complex activity**

88 Although it was previously reported that inhibiting teichoic acid synthesis does not affect the
89 activity/motion of Rod complexes at steady-state[6,7], we hypothesized that loss of cell shape results from
90 a quantitative or transient effect of teichoic acid depletion on Rod complex activity. To test this, we
91 used total internal reflection fluorescence microscopy to measure the effect of tunicamycin on the
92 temporal dependence of Rod complex motion in cells expressing a fluorescent version of Mbl (Mbl-
93 sfGFP)[23,28,29]. As we hypothesized, tunicamycin caused an acute decrease in the percentage of Rod
94 complexes that moved processively, (Fig. 1C), in the spatial density of processive Rod complexes (Fig.

95 S3A), and in Rod complex speed (Fig. S3B). These decreases were coincident with the first decline in
96 cellular growth rate (Fig. 1B). However, following the second decrease in growth rate (and loss of cell
97 shape; Fig. 1B) we observed a small but reproducible recovery of Rod complex motion (Fig. 1C),
98 consistent with the previous observation of Rod complex motion in *ΔtagO* mutants[6]. Visual inspection of
99 cells treated with tunicamycin for 60 minutes confirmed the presence of oriented Rod complex motion,
100 but with a high level of spatially diffuse Mbl-sfGFP fluorescence relative to untreated cells (Fig. S3C,
101 Videos S2-S7). Tunicamycin treatment also inhibited Rod complex motion as measured with an MreB-
102 mNeonGreen fusion (Figs. S3D-F), demonstrating that this effect is not specific to a single species of Rod
103 complex. Finally, transcriptional inhibition of *tagO* caused a decrease in each metric associated with Rod
104 complex activity (Fig. S3G-I). This decrease was more gradual in the case of transcriptional inhibition,
105 which is expected since in this case TagO enzymes must be diluted by growth before teichoic acids are
106 depleted.

107

108 Although Rod complex motion depends on peptidoglycan synthesis, in principle it is possible that Rod
109 complexes could synthesize peptidoglycan without moving. To test this, we measured the rate at which
110 the fluorescent D-amino acid HADA (7-hydroxycoumarin-3-carboxylic acid-amino-D-alanine) was
111 incorporated into the cell wall upon teichoic acid depletion. We perfused cells with HADA for 5 minutes
112 at a range of times after tunicamycin treatment and, following wash-out, we measured the average
113 fluorescence intensity within the cell envelope as a proxy for cross-linking by the Rod complexes[47,48].
114 Tunicamycin caused a rapid decrease in the rate of HADA incorporation (Fig. 1D). Furthermore, whereas
115 HADA labeled the cell wall of untreated cells uniformly (Fig. 1Di), 30 minutes of tunicamycin treatment
116 caused aberrant, punctate labeling (Fig. 1Diii). We obtained similar results for Δ*ponA* and Δ*dacA*
117 mutants, demonstrating that the decrease in HADA incorporation does not reflect inhibition of PBP1 or
118 activation of the major D,D-carboxypeptidase DacA, which removes HADA[49]. Similarly, transcriptional

119 inhibition of TagO expression caused a reduction in HADA incorporation (Fig. S4A). Finally, we found
120 that deleting *tagO* caused a reduction in the total concentration of cell wall cross-links, as measured
121 through high performance liquid chromatography analysis of purified cell walls[49] (Fig. S4B,C). In
122 summary, Rod complex activity decreases upon teichoic acid depletion, coincident with a PBP1-
123 independent decrease in HADA incorporation.

124

125 **PBP1 is essential in the absence of wall teichoic acid synthesis**

126 Since i) Rod complexes and PBP1 are the two principal modes of peptidoglycan synthesis during cell
127 growth, ii) teichoic acid depletion acutely inhibits Rod complex activity (Fig. 1C), and iii) the resulting
128 growth is amorphous as would be expected from PBP1-mediated cell growth, we hypothesized that
129 teichoic acid-less growth is primarily driven by PBP1. To test this, we first measured the effect of
130 tunicamycin treatment on the growth, shape, and Rod complex activity of Δ*ponA* mutants. At the single-
131 cell level, tunicamycin caused a decrease in the growth rate of Δ*ponA* cells, similar to the growth-rate
132 decrease it caused in wild-type cells except without the transient plateau and subsequent shape loss
133 (Fig. 2A). In contrast to wild-type cells, Δ*ponA* mutants exhibited pervasive lysis after their growth rate
134 decrease (Fig. 2B). Similarly, in bulk liquid culture, sublethal concentrations of tunicamycin that
135 permitted amorphous growth in wild-type cells completely inhibited growth in Δ*ponA* cells (Fig. 2C).
136 Teichoic acid-less growth required the transpeptidase activity of PBP1 since a transpeptidase mutant
137 $ponA^{TP-}$ (Fig. S5A) that we constructed[50] was also fully inhibited at this tunicamycin concentration (Fig.
138 2C). Like tunicamycin, transcriptional inhibition of *tagO* expression also prevented growth of Δ*ponA* and
139 $ponA^{TP-}$ mutants on solid media (Fig. S5B). Finally, as for wild-type cells, tunicamycin decreased Rod
140 complex motion in Δ*ponA* mutant cells except with a modest delay (Fig. 2D).

141

142 Together, these results demonstrate that PBP1 is responsible for amorphous cell growth following
143 teichoic acid depletion, which inhibits Rod complexes. We hypothesized that PBP1 activity would
144 increase to compensate for the lack of Rod complex-mediated synthesis during teichoic acid depletion.
145 To test this, we treated exponentially growing bulk liquid cultures with tunicamycin and measured the
146 temporal dynamics of labeling by a fluorescent penicillin, which covalently binds to active
147 transpeptidases[51]. We found that tunicamycin caused a rapid ≈30% increase in PBP1 labeling relative to
148 the combined labeling of PBP2A and the cell division peptidoglycan synthase PBP2B (which are not
149 distinguished by this assay; Figs. 2E,F). The increase in PBP1 labeling could reflect increased protein
150 levels and/or specific activity. However, based on previous studies[1], an increase in PBP1 protein levels of
151 this magnitude is not alone sufficient to the cell shape changes we observe. These results are therefore
152 consistent with a model in which teichoic acids directly inhibit PBP1 activity. In this model, increased
153 PBP1 activity, combined with the simultaneous inhibition of Rod complex activity, leads to slow,
154 amorphous cell growth. Furthermore, increased PBP1 activity would contribute to Rod complex
155 inhibition if the two modes of peptidoglycan synthesis were competing for lipid II precursors or peptide
156 acceptors (*Discussion*).

157

158 **Teichoic acid depletion results in irrevocable cell wall damage in the absence of PBP1**

159 Since PBP1 is thought to fill pores in the cell wall[4] and is conditionally essential in the absence of teichoic
160 acids, we hypothesized that teichoic acids play a complementary pore-filling role and that Rod
161 complexes require a pore-less "confluent" cell wall on which to synthesize new peptidoglycan. A
162 previous genetic analysis predicted that PBP1 is activated by cell wall damage, which could be sensed
163 through PBP1's intrinsically disordered domain[33]. Therefore, we additionally hypothesized that PBP1
164 synthesizes peptidoglycan to "repair" the same incipient pores exposed by teichoic acid depletion.

165

166 To test whether depletion of teichoic acids results in pores within the cell wall, we used a single-cell
167 microfluidics assay we recently developed. In this assay, we used brief pulses of detergent to lyse cells
168 expressing genetically encoded, cytosolic fluorescent probes and then measured the kinetics of the
169 probes' diffusion through the cell wall at the single-cell level — this provides an empirical measurement
170 of cell wall permeability (*Methods*). To test for pores of different sizes, we used two probes:
171 mNeonGreen (27.5 kDa, minimal radius R_{min}≈2.0nm[52]) and a fluorogenic version of ubiquitin (9.5 kDa,
172 R_{min}≈1.4nm) .

173

174 We first measured the effect of teichoic acid depletion on cell wall permeability by treating wild-type
175 and Δ*ponA* cells with tunicamycin (Figs. 1C,2D). To avoid the potential for confounding changes in
176 peptidoglycan synthesis on cell wall permeability, we treated cells for as long as possible before Rod
177 complex activity began to decline (10 min and 20 min for WT and Δ*ponA*). Contrary to our initial
178 expectations, tunicamycin treatment of wild-type cells resulted in a modest but reproducible decrease
179 in the permeability of wild-type cell walls, as measured with the mNeonGreen probe (Fig. 3A).
180 Conversely, the same treatment resulted in an increase in permeability in Δ*ponA* cells. As an alternative
181 approach to remove teichoic acids, we perfused cells with a purified phosphodiesterase, GlpQ, that *B.*
182 *subtilis* naturally expresses during phosphate starvation to digest and recycle its teichoic acids[53]
183 (*Methods*). Perfusing cells with GlpQ for 15 minutes strongly reduced the abundance of teichoic acids
184 within the cell wall (Fig. S6) (*Methods*) and recapitulated the effect of tunicamycin on cell wall
185 permeability: it caused a modest decrease in mNeonGreen permeability in wild-type cells but a large
186 increase in permeability in Δ*ponA* cells (Fig. 3B). Together, these results are consistent with a model in

187 which teichoic acids occlude pores in the cell wall, and in which PBP1 fills these pores with
188 peptidoglycan that is intrinsically less porous than the cell wall synthesized by untreated wild-type cells.

189

190 Treatment of Δ*ponA* cells with tunicamycin or GlpQ for periods of time that approach the cell-cycle time
191 (≈20 min) could induce pore formation indirectly, for example, through unbalanced peptidoglycan
192 hydrolysis[8–11]. To control for this possibility, we measured cell-wall permeability during teichoic acid
193 digestion by GlpQ, reasoning that at very short time scales after teichoic acid digestion, peptidoglycan
194 hydrolases would not have had time to meaningfully enlarge pores. Because we anticipated that we
195 were looking for small, incipient pores, we used our ubiquitin probe to test for them. When we
196 simultaneously digested teichoic acids and measured the loss of this probe in Δ*ponA* cells, we observed
197 a reproducible increase in cell wall permeability within 1 minute of GlpQ treatment (Figs. 3C,S7A,B).

198

199 We reasoned that the nascent pores exposed during teichoic acid depletion would cause higher labeling
200 by peptidoglycan-binding ligands. To test this, we measured whether teichoic acid depletion affected
201 cell-wall labeling with a fluorescent lectin that specifically binds to the N-acetyl glucosamine moiety of
202 peptidoglycan. We observed a reproducible increase in labeling of both Δ*ponA* cells and, to a lesser
203 extent, in wild-type cells following pre-treatment with tunicamycin (Fig. S7C). We propose that teichoic
204 acid depletion reduces permeability (Fig. 3A) but increases lectin binding in wild-type cells because PBP1
205 is membrane-bound and would therefore only fill pores on the internal surface of the cell wall, leaving
206 teichoic acid-less peptidoglycan on the outer surface exposed.

207

208 Since PBP1 complements the effect of teichoic acids on cell wall permeability, we reasoned that
209 enzymatically removing teichoic acids from Δ*ponA* cells would inhibit cell growth recovery upon re-
210 immersion in growth media. To test this, we cultured bacteria to steady-state exponential growth in
211 rich media, induced pore formation by digesting teichoic acids with GlpQ (suspended in PBS, which also
212 arrested cell growth), and then monitored the growth recovery upon re-perfusion of rich media. As
213 hypothesized, Δ*ponA* cells were unable to recover from teichoic acid digestion but did not lyse (Fig. 3D),
214 whereas wild-type cells that possessed PBP1 partially recovered (Fig. 3E). Furthermore, wild-type cells
215 that resumed growth did so as rods and showed a full recovery of Rod complex activity (Fig. 3Ei,iii),
216 while cells that remained arrested showed no Rod complex motion (Figs. 3Eii,iv,S8A-D). Rod complex
217 activity and cell growth of both wild-type and Δ*ponA* cells recovered fully from incubation in PBS alone
218 (Fig. S8E-G, S9A,B). This correlation between pores, Rod complex activity and PBP1 is strong evidence
219 that the Rod complex is incapable of adding peptidoglycan to a porous cell wall. However, since GlpQ-
220 treatment of wild-type cells does not induce pores (Fig. 3C) but partially inhibits growth recovery (Fig.
221 3E), teichoic acid digestion must additionally inhibit cell growth via a mechanism independent of pores,
222 at least of those that are detected by the mNeonGreen probe.

223

224 Finally, we reasoned that if cell wall pores inhibit Rod complex activity upon teichoic acid removal, then
225 shrinking these pores would activate Rod complexes, thereby promoting cell growth recovery after GlpQ
226 treatment. We tested this prediction by coupling the exit from GlpQ treatment to a 500 mM
227 hyperosmotic shock to physically contract the cell wall[54]. To ensure that any cell growth recovery
228 resulted directly from cell wall contraction and not from PBP1 activity, we performed this experiment in
229 Δ*ponA* cells that are otherwise unable to grow following teichoic acid cleavage. Consistent with our
230 hypothesis, we observed a partial growth recovery following the hyperosmotic shock (Fig. 3F, S9C).

231

232 **Discussion**

233 Our data support a model in which teichoic acids occlude nanoscopic pores in peptidoglycan (Fig. 4A,B).
234 We propose that in wild-type cells, teichoic acids limit PBP1's access to the inner face of the cell wall via
235 these pores, which lowers the enzyme's absolute activity. When teichoic acids are depleted, these pores
236 are exposed and PBP1 activity increases (Fig. 2F), promoting amorphous growth. This model is
237 consistent with a previous study showing that PBP1 activity is stimulated by its long intrinsically
238 disordered domain upon cell wall damage[33], a signal that would be induced by nascent pores if teichoic
239 acids excluded this domain from the cell wall via the same type of polymer-polymer interactions that
240 underlie macromolecular crowding[55].

241

242 On a slightly slower time scale, teichoic acid depletion causes decreased activity of Rod complexes (Fig.
243 1C). In wild-type cells, we find it likely that this occurs for two reasons. First, PBP1 activity will reduce
244 the pool of lipid II available for Rod complexes if the synthesis of lipid II is rate-limiting for cell wall
245 synthesis, which is expected during fast cell growth. Second, if increased PBP1 synthesis is targeted to
246 discrete pores, then this could result in a heterogeneous distribution of nascent peptide acceptors in the
247 cell wall to which Rod complexes can add material. This is consistent with the highly punctate synthesis
248 patterns we observe upon tunicamycin treatment (Fig. 1D). If this heterogeneity becomes too large,
249 Rod complexes will arrest when they encounter areas without acceptors for the same reason that
250 pharmacological inhibition of Class B PBP transpeptidation arrests Rod complexes[23–25]. The localized
251 pattern of peptide acceptors would not be inhibitory to PBP1 since it i) is not spatially processive and ii)
252 can cross-link to the peptides that it makes itself, which would reinforce localized synthesis.

253

254 Consistent with the latter mechanism, in the absence of PBP1 (Δ*ponA*), teichoic acid depletion
255 simultaneously causes the formation of large pores in the cell wall (Fig. 3A,B) and the eventual arrest of
256 Rod complexes (Figs. 2D,3D). We propose that the nascent pores exposed by teichoic acid depletion
257 enlarge without repair by PBP1 (Fig. 4A). When the pores become too large, the density of peptide
258 acceptors becomes prohibitively low for Rod complex procession. The delay in Rod complex arrest in
259 Δ*ponA* mutants compared to that in wild-type cells is expected without direct competition from PBP1.
260 Given this model, one role of PBP1 at wild-type (low) activity may be to provide a lawn of nascent
261 peptide acceptors for Rod complexes.

262

263 Finally, our model can account for why Rod complex activity partially recovers at late times after teichoic
264 acid depletion, and in Δ*tagO* mutants. The transition from thin rods, to wide rods, to amorphous
265 spheroids directly lowers the surface area-to-volume ratio of the cells, which is expected to restore lipid
266 II levels by lowering the fraction of metabolic flux, per unit cell volume, needed for cell wall expansion.
267 Rod complexes therefore become partially active again, but not at a high enough level to confer rod
268 shape since PBP1 is constitutively de-inhibited and still directs peptidoglycan synthesis to nascent,
269 teichoic acid-less pores.

270

271 In addition to cell wall synthesis, teichoic acids also influence peptidoglycan hydrolysis during cell
272 growth, both directly and indirectly[8–11]. For example, teichoic acid depletion increases the expression of
273 the key hydrolase LytE[12] via the anti-sigma factor RsgI, a pathway that is activated by cell wall damage
274 via RsgI's intrinsically disordered domain[33]. In this light, we predict that the large holes that form in the
275 walls of teichoic acid-less cells that are incubated in buffer arise from increased, aberrant hydrolysis (i.e.
276 autolysis). Teichoic acids' influence on hydrolysis could underlie our observation that GlpQ-mediated

277 digestion of teichoic acids partially prevents recovery of wild-type cells even though PBP1 activity
278 prevents the formation of large pores (Fig. 3E). For example, runaway hydrolysis and PBP1 activity
279 during GlpQ treatment could create an irreversibly altered cell wall incapable of supporting growth.

280

281 In sum, wall teichoic acids lie at the center of a feedback system that modulates both modes of
282 peptidoglycan synthesis as well as its hydrolysis, positioning them as "master regulators" of rod-shaped
283 morphogenesis in Gram-positive bacteria. Our study resolves the longstanding question of how teichoic
284 acids promote rod-shape without directly contributing to cell wall anisotropy. Furthermore, we establish
285 a direct link between the physical architecture of the cell wall and anisotropic cell wall synthesis,
286 identifying the cell wall as a critical autoregulatory factor of its own synthesis, rather than a passive
287 substrate.

288 **References**

289 1. Dion, M. F. *et al.* Bacillus subtilis cell diameter is determined by the opposing actions of two distinct
290 cell wall synthetic systems. *Nature Microbiology* **4**, 1294–1305 (2019).
291 2. Garner, E. C. Toward a Mechanistic Understanding of Bacterial Rod Shape Formation and
292 Regulation. *Annual Review of Cell and Developmental Biology* **37**, null (2021).
293 3. Young, K. D. The Selective Value of Bacterial Shape. *Microbiology and Molecular Biology Reviews* **70**,
294 660–703 (2006).
295 4. Cho, H. *et al.* Bacterial cell wall biogenesis is mediated by SEDS and PBP polymerase families
296 functioning semi-autonomously. *Nat Microbiol* **1**, 1–8 (2016).
297 5. D'Elia, M. A., Millar, K. E., Beveridge, T. J. & Brown, E. D. Wall Teichoic Acid Polymers Are
298 Dispensable for Cell Viability in Bacillus subtilis. *Journal of Bacteriology* **188**, 8313–8316 (2006).
299 6. Hussain, S. *et al.* MreB filaments align along greatest principal membrane curvature to orient cell
300 wall synthesis. *eLife* **7**, e32471 (2018).
301 7. Schirner, K. *et al.* Lipid-linked cell wall precursors regulate membrane association of bacterial actin
302 MreB. *Nature Chemical Biology* **11**, 38–45 (2015).
303 8. Bonnet, J. *et al.* Nascent teichoic acids insertion into the cell wall directs the localization and activity
304 of the major pneumococcal autolysin LytA. *The Cell Surface* **2**, 24–37 (2018).
305 9. Wecke, J., Perego, M. & Fischer, W. d-Alanine Deprivation of Bacillus subtilis Teichoic Acids Is
306 without Effect on Cell Growth and Morphology But Affects the Autolytic Activity. *Microbial Drug*
307 *Resistance* **2**, 123–129 (1996).
308 10. Flores-Kim, J., Dobihal, G. S., Fenton, A., Rudner, D. Z. & Bernhardt, T. G. A switch in surface polymer
309 biogenesis triggers growth-phase-dependent and antibiotic-induced bacteriolysis. *eLife* **8**, e44912
310 (2019).

311 11. Flores-Kim, J., Dobihal, G. S., Bernhardt, T. G. & Rudner, D. Z. WhyD tailors surface polymers to
312 prevent premature bacteriolysis and direct cell elongation in Streptococcus pneumoniae. *eLife* **11**,
313 e76392 (2022).
314 12. Kasahara, J. *et al.* Teichoic Acid Polymers Affect Expression and Localization of dl-Endopeptidase
315 LytE Required for Lateral Cell Wall Hydrolysis in Bacillus subtilis. *Journal of Bacteriology* **198**, 1585–
316 1594 (2016).
317 13. Yamamoto, H., Miyake, Y., Hisaoka, M., Kurosawa, S.-I. & Sekiguchi, J. The major and minor wall
318 teichoic acids prevent the sidewall localization of vegetative DL-endopeptidase LytF in Bacillus
319 subtilis. *Mol Microbiol* **70**, 297–310 (2008).
320 14. Goldman, W. E., Klapper, D. G. & Baseman, J. B. Detection, isolation, and analysis of a released
321 Bordetella pertussis product toxic to cultured tracheal cells. *Infection and Immunity* **36**, 782–794
322 (1982).
323 15. Sassine, J. *et al.* Functional redundancy of division specific penicillin-binding proteins in Bacillus
324 subtilis. *Molecular Microbiology* **106**, 304–318 (2017).
325 16. Barber, F., Min, J., Murray, A. W. & Amir, A. Modeling the impact of single-cell stochasticity and size
326 control on the population growth rate in asymmetrically dividing cells. *PLOS Computational Biology*
327 **17**, e1009080 (2021).
328 17. Barber, F., Ho, P.-Y., Murray, A. W. & Amir, A. Details Matter: Noise and Model Structure Set the
329 Relationship between Cell Size and Cell Cycle Timing. *Frontiers in Cell and Developmental Biology* **5**,
330 (2017).
331 18. Chang, F. & Huang, K. C. How and why cells grow as rods. *BMC Biol* **12**, 54 (2014).
332 19. Armstrong, J. J., Baddiley, J., Buchanan, J. G. & Carss, B. Nucleotides and the Bacterial Cell Wall.
333 *Nature* **181**, 1692–1693 (1958).

334 20. Armstrong, J. J. *et al.* Teichoic Acids from Bacterial Walls: Composition of Teichoic Acids from a
335 Number of Bacterial Walls. *Nature* **184**, 247–248 (1959).
336 21. Boylan, R. J., Mendelson, N. H., Brooks, D. & Young, F. E. Regulation of the Bacterial Cell Wall:
337 Analysis of a Mutant of Bacillus subtilis Defective in Biosynthesis of Teichoic Acid. *Journal of*
338 *Bacteriology* **110**, 281–290 (1972).
339 22. Eugster, M. R. & Loessner, M. J. Wall Teichoic Acids Restrict Access of Bacteriophage Endolysin
340 Ply118, Ply511, and PlyP40 Cell Wall Binding Domains to the Listeria monocytogenes Peptidoglycan.
341 *J Bacteriol* **194**, 6498–6506 (2012).
342 23. Garner, E. C. *et al.* Coupled, Circumferential Motions of the Cell Wall Synthesis Machinery and MreB
343 Filaments in B. subtilis. *Science* **333**, 222–225 (2011).
344 24. van Teeffelen, S. *et al.* The bacterial actin MreB rotates, and rotation depends on cell-wall assembly.
345 *Proceedings of the National Academy of Sciences* **108**, 15822–15827 (2011).
346 25. Domínguez-Escobar, J. *et al.* Processive Movement of MreB-Associated Cell Wall Biosynthetic
347 Complexes in Bacteria. *Science* **333**, 225–228 (2011).
348 26. Carballido-López, R. *et al.* Actin homolog MreBH governs cell morphogenesis by localization of the
349 cell wall hydrolase LytE. *Dev Cell* **11**, 399–409 (2006).
350 27. Daniel, R. A. & Errington, J. Control of cell morphogenesis in bacteria: two distinct ways to make a
351 rod-shaped cell. *Cell* **113**, 767–776 (2003).
352 28. Billaudeau, C. *et al.* Contrasting mechanisms of growth in two model rod-shaped bacteria. *Nature*
353 *Communications* **8**, 15370 (2017).
354 29. Sun, Y., Hürlimann, S. & Garner, E. Growth rate is modulated by monitoring cell wall precursors in
355 Bacillus subtilis. *Nat Microbiol* **8**, 469–480 (2023).
356 30. Meeske, A. J. *et al.* SEDS proteins are a widespread family of bacterial cell wall polymerases. *Nature*
357 **537**, 634–638 (2016).

358 31. Wei, Y., Havasy, T., McPherson, D. C. & Popham, D. L. Rod Shape Determination by the Bacillus
359 subtilis Class B Penicillin-Binding Proteins Encoded by pbpA and pbpH. *Journal of Bacteriology* **185**,
360 4717–4726 (2003).
361 32. McPherson, D. C. & Popham, D. L. Peptidoglycan Synthesis in the Absence of Class A Penicillin-
362 Binding Proteins in Bacillus subtilis. *Journal of Bacteriology* **185**, 1423–1431 (2003).
363 33. Brunet, Y. R., Habib, C., Brogan, A. P., Artzi, L. & Rudner, D. Z. Intrinsically disordered protein regions
364 are required for cell wall homeostasis in Bacillus subtilis. *Genes Dev* **36**, 970–984 (2022).
365 34. Brown, S. *et al.* Methicillin resistance in Staphylococcus aureus requires glycosylated wall teichoic
366 acids. *Proc Natl Acad Sci U S A* **109**, 18909–18914 (2012).
367 35. Campbell, J. *et al.* Synthetic Lethal Compound Combinations Reveal a Fundamental Connection
368 between Wall Teichoic Acid and Peptidoglycan Biosyntheses in Staphylococcus aureus. *ACS Chem.*
369 *Biol.* **6**, 106–116 (2011).
370 36. Farha, M. A. *et al.* Inhibition of WTA Synthesis Blocks the Cooperative Action of PBPs and Sensitizes
371 MRSA to beta-Lactams. *ACS Chem. Biol.* **8**, 226–233 (2013).
372 37. Lu, Y. *et al.* Modulation of MRSA virulence gene expression by the wall teichoic acid enzyme TarO.
373 *Nat Commun* **14**, 1594 (2023).
374 38. Thomas, K. J. & Rice, C. V. Equilibrium binding behavior of magnesium to wall teichoic acid.
375 *Biochimica et Biophysica Acta (BBA) - Biomembranes* **1848**, 1981–1987 (2015).
376 39. Wecke, J., Madela, K. & Fischer, W. The absence of D-alanine from lipoteichoic acid and wall teichoic
377 acid alters surface charge, enhances autolysis and increases susceptibility to methicillin in Bacillus
378 subtilis. *Microbiology (Reading)* **143**, 2953–2960 (1997).
379 40. Atilano, M. L. *et al.* Teichoic acids are temporal and spatial regulators of peptidoglycan cross-linking
380 in Staphylococcus aureus. *PNAS* **107**, 18991–18996 (2010).

381 41. Formstone, A., Carballido-López, R., Noirot, P., Errington, J. & Scheffers, D.-J. Localization and
382 Interactions of Teichoic Acid Synthetic Enzymes in Bacillus subtilis. *Journal of Bacteriology* **190**,
383 1812–1821 (2008).
384 42. Koyano, Y., Okajima, K., Mihara, M. & Yamamoto, H. Visualization of Wall Teichoic Acid Decoration
385 in Bacillus subtilis. *Journal of Bacteriology* **0**, e00066-23 (2023).
386 43. Bonnet, J. *et al.* One-Pot Two-Step Metabolic Labeling of Teichoic Acids and Direct Labeling of
387 Peptidoglycan Reveals Tight Coordination of Both Polymers Inserted into Pneumococcus Cell Wall.
388 *ACS Chem. Biol.* **13**, 2010–2015 (2018).
389 44. Bracha, R. & Glaser, L. An intermediate in teichoic acid biosynthesis. *Biochemical and Biophysical*
390 *Research Communications* **72**, 1091–1098 (1976).
391 45. Hancock, I. C., Wiseman, G. & Baddiley, J. Biosynthesis of the unit that links teichoic acid to the
392 bacterial wall: Inhibition by tunicamycin. *FEBS Letters* **69**, 75–80 (1976).
393 46. Mirouze, N., Ferret, C., Cornilleau, C. & Carballido-López, R. Antibiotic sensitivity reveals that wall
394 teichoic acids mediate DNA binding during competence in Bacillus subtilis. *Nat Commun* **9**, 5072
395 (2018).
396 47. Hsu, Y.-P. *et al.* Fluorogenic d -amino acids enable real-time monitoring of peptidoglycan
397 biosynthesis and high-throughput transpeptidation assays. *Nature Chemistry* **11**, 335–341 (2019).
398 48. Lupoli, T. J. *et al.* Transpeptidase-Mediated Incorporation of d-Amino Acids into Bacterial
399 Peptidoglycan. *J. Am. Chem. Soc.* **133**, 10748–10751 (2011).
400 49. Atrih, A., Bacher, G., Allmaier, G., Williamson, M. P. & Foster, S. J. Analysis of peptidoglycan
401 structure from vegetative cells of Bacillus subtilis 168 and role of PBP 5 in peptidoglycan maturation.
402 *J Bacteriol* **181**, 3956–3966 (1999).
403 50. Sauvage, E. & Terrak, M. Glycosyltransferases and Transpeptidases/Penicillin-Binding Proteins:
404 Valuable Targets for New Antibacterials. *Antibiotics* **5**, 12 (2016).

405 51. Sharifzadeh, S., Dempwolff, F., Kearns, D. B. & Carlson, E. E. Harnessing β-Lactam Antibiotics for
406 Illumination of the Activity of Penicillin-Binding Proteins in Bacillus subtilis. *ACS Chem. Biol.* **15**,
407 1242–1251 (2020).
408 52. Erickson, H. P. Size and Shape of Protein Molecules at the Nanometer Level Determined by
409 Sedimentation, Gel Filtration, and Electron Microscopy. *Biol Proced Online* **11**, 32–51 (2009).
410 53. Myers, C. L. *et al.* Identification of Two Phosphate Starvation-induced Wall Teichoic Acid Hydrolases
411 Provides First Insights into the Degradative Pathway of a Key Bacterial Cell Wall Component*.
412 *Journal of Biological Chemistry* **291**, 26066–26082 (2016).
413 54. Bardetti, P., Barber, F. & Rojas, E. R. Non-linear stress-softening of the bacterial cell wall confers cell
414 shape homeostasis. 2024.09.03.611099 Preprint at https://doi.org/10.1101/2024.09.03.611099
415 (2024).
416 55. Delarue, M. *et al.* mTORC1 Controls Phase Separation and the Biophysical Properties of the
417 Cytoplasm by Tuning Crowding. *Cell* **174**, 338-349.e20 (2018).
418

419 **Figures**

420

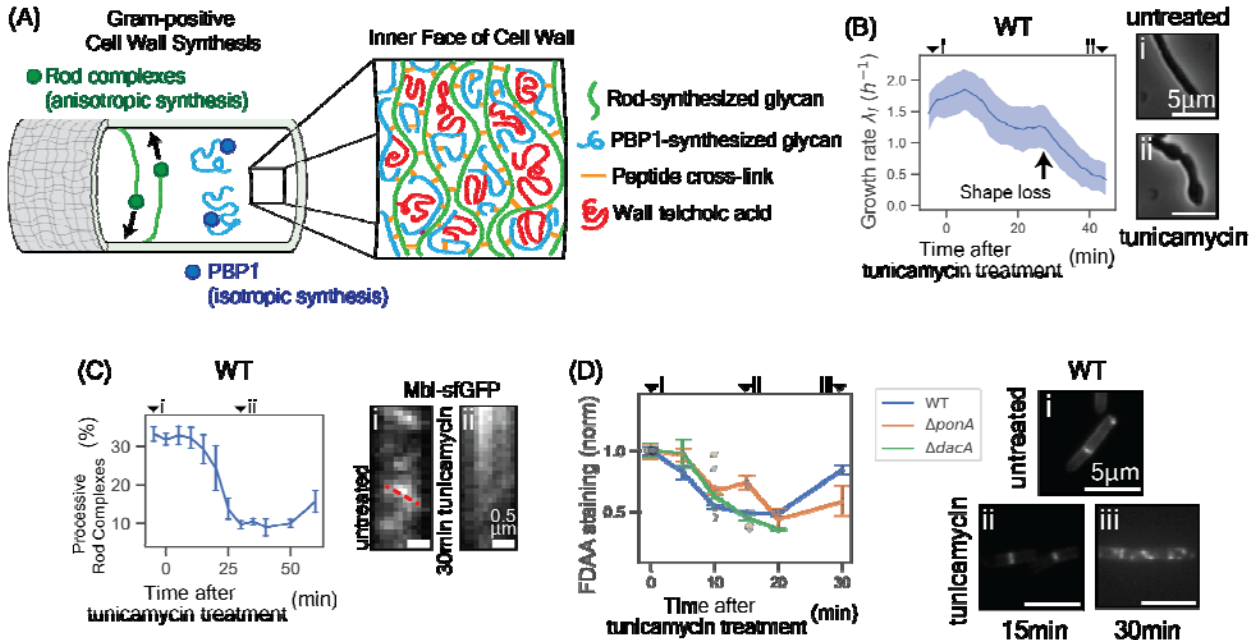

421

422 **Fig. 1: Inhibiting wall teichoic acid synthesis decreases Rod complex activity prior to cell shape loss. (A)**

423 Schematic of Gram-positive cell wall synthesis. **(B)** Cell length growth rate −— for wild-type cells

424 during 0.5 g/mL tunicamycin treatment. Blue line shows smoothed population median, error bars show

425 standard deviation. Analysis performed over 2,048 discrete cell tracks from 3 biological replicates. Inset:

426 micrographs taken (i) before and (ii) after 45 min tunicamycin treatment as shown by black arrows. Scale

427 bars 5 m. **(C)** Time course showing the percentage of processive Mbl filaments during a 0.5 g/mL

428 tunicamycin treatment. Error bars show 95% confidence intervals across biological replicates based on

429 bootstrap analysis. Analysis performed on 62,901 discrete filament tracks from 4 biological replicates.

430 Inset shows representative fluorescent kymographs of Mbl motion across the cell waist in (i) LB and (ii)

431 after 30 min tunicamycin treatment as shown by black arrows. Red dotted line follows a processive Mbl

432 filament. Scale bars 1 m. **(D)** Normalized mean cell envelope HADA staining for wild-type, Δ*ponA* and

433 Δ*dacA* cells during tunicamycin treatment. Error bars show 95% confidence intervals. Analysis

434 performed over 3,458 segmentations from 3 biological replicates (wild-type), 1,664 segmentations from

435 two biological replicates (Δ*ponA*), and 2,440 segmentations from 3 biological replicates (Δ*dacA*). Dots

436 show individual replicates. Inset shows identically saturated micrographs of wild-type cells at (i) 0 min,

437 (ii) 15 min, and (iii) 30 min of treatment.

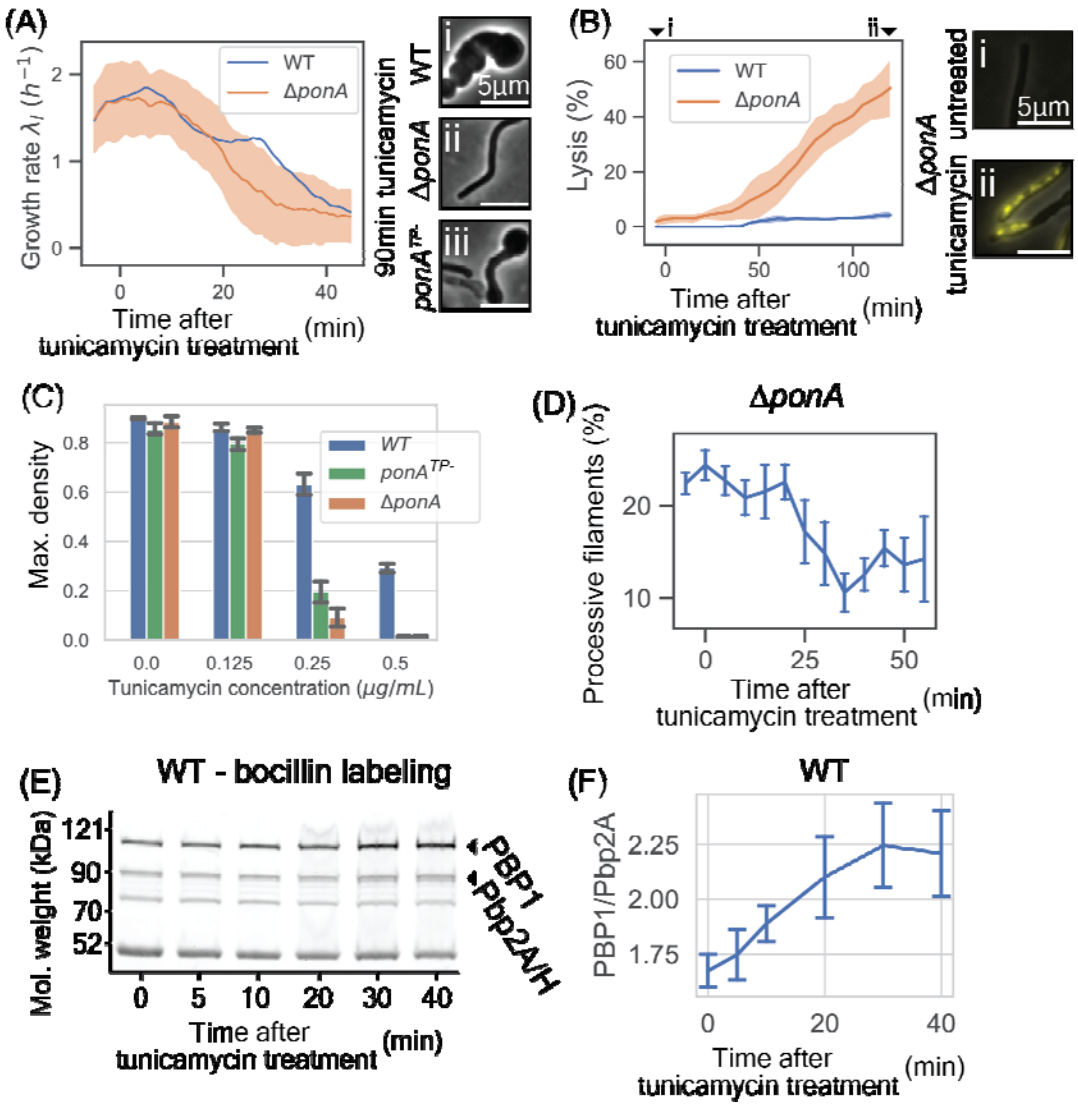

Figure 2: PBP1 is required for growth during wall teichoic acid synthesis inhibition. (A) Cell length growth rate –— for Δ*ponA* cells during 0.5 g/mL tunicamycin treatment. Blue line shows smoothed population median, error bars show standard deviation. Analysis performed over 621 discrete cell tracks from 5 biological replicates. Blue line reproduces wild-type data from Fig. 1A. Inset: micrographs showing (i) wild-type, (ii) Δ*ponA* and (iii) *ponA*$^{TP-}$ cells following 90 min treatment with 0.5 g/mL tunicamycin. Scale bar 5 m. **(B)** Percentage of membrane-disrupted cells following tunicamycin exposure, measured by propidium iodide staining. Solid line shows mean across all fields of view. Error bars show standard deviation of the same. Analysis performed over 1,098 cells from three biological replicates (Δ*ponA*) and 896 cells from one biological replicate (wild-type). Inset: micrographs showing *ΔponA* cells (i) before and (ii) after 2h tunicamycin treatment. Phase overlaid with propidium iodide stain. Scale bars 5 m. **(C)** Maximum OD for wild-type, Δ*ponA* and *ponA*$^{TP-}$ (expressing PBP1 with an

450 inactive transpeptidase domain) in varying doses of tunicamycin, grown in bulk culture. Data shown
451 from one representative biological replicate out of three, with four technical replicates per biological
452 replicate. **(D)** Percentage of processive Mbl-sfGFP filaments during tunicamycin treatment of *ΔponA*
453 cells. Error bars show 95% confidence intervals across biological replicates based on bootstrap analysis.
454 Analysis performed on 40,793 discrete filament tracks from three biological replicates. **(E)** SDS-PAGE of
455 *B. subtilis* whole cell lysates shows PBP activity levels during tunicamycin treatment. Arrows show (i)
456 PBP1 and (ii) PBP2A/PBP2B bands. Cells treated with fluorescent bocillin for two minutes prior to cell
457 lysis. One representative sample shown from 4 biological replicates. **(F)** Quantification of (E), showing
458 the ratio of PBP1 to PBP2A/PBP2B intensity. Error bars show standard error of the mean across
459 replicates.

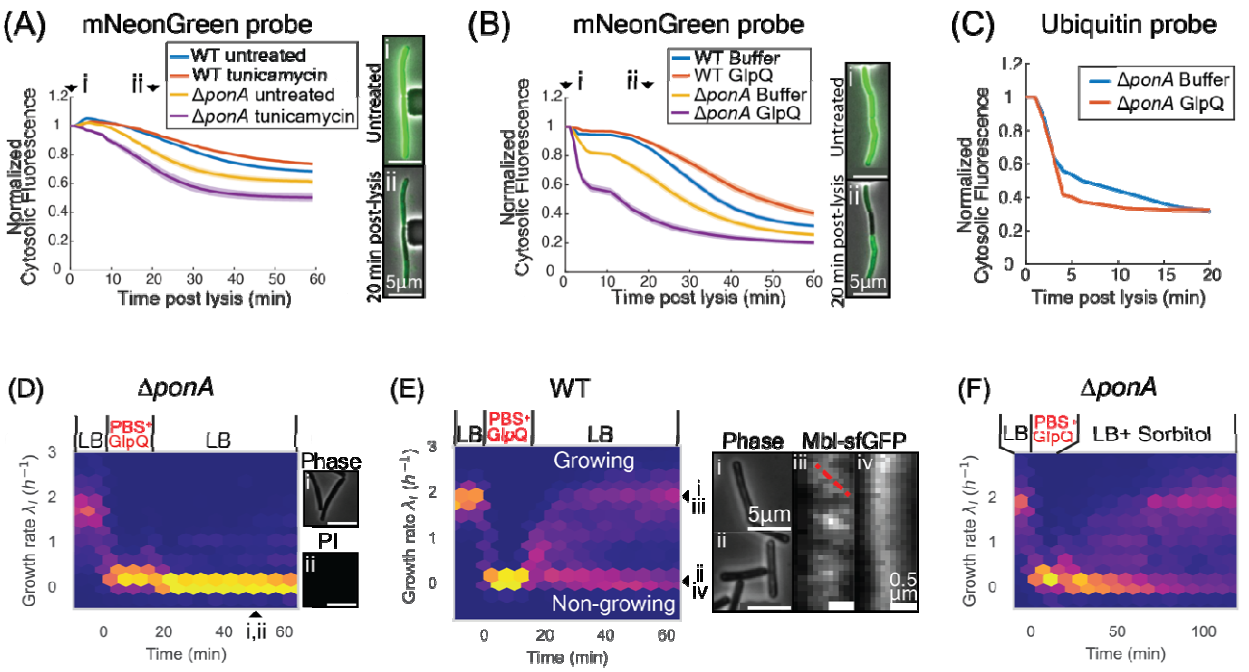

Figure 3: PBP1 fills pores that are exposed upon wall teichoic acid removal, conferring growth. (A) mNeonGreen diffusion out of lysed cells following a 10 min (wild-type) or 20 min (Δ*ponA*) incubation with LB supplemented with tunicamycin or with LB alone. Wild-type untreated: 87 cells, 4 biological replicates. Wild-type tunicamycin: 139 cells, 3 biological replicates. Δ*ponA* untreated: 53 cells, 3 biological replicates. Δ*ponA* tunicamycin: 35 cells, 3 biological replicates. Inset: micrographs showing cellular fluorescence of tunicamycin-treated Δ*ponA* cells (i) before and (ii) 20 min after cell lysis. Scale bars 5 m. **(B)** mNeonGreen diffusion out of lysed wild-type and Δ*ponA* cells following a 15-minute live-cell incubation with PBS supplemented with either 40 M GlpQ in Buffer A or with Buffer A alone. Wild-type Buffer: 121 cells, 1 biological replicate. Wild-type GlpQ: 90 cells, 1 biological replicate. Δ*ponA* Buffer: 85 cells, 3 biological replicates. Δ*ponA* GlpQ: 108 cells, 3 biological replicates. Inset: micrographs showing cellular fluorescence of GlpQ-treated Δ*ponA* cells (i) before and (ii) 20 min after cell lysis. Scale bars 5 m. **(C)** Ubiquitin-FlAsH diffusion out of lysed Δ*ponA* cells following a 2 min incubation with PBS +5% N-lauroylsarcosine + either 40 M GlpQ or the equivalent volume of Buffer A. **(D)** Heat map showing growth rate −— of Δ*ponA* cells following a 15 min incubation with 10 M native GlpQ cells (1,816 discrete tracks, 3 biological replicates). Heat map intensity is proportional to the number of cells with a given growth rate at a given time, normalized across the total number of cells tracked at each timepoint. Inset: lack of propidium iodide staining for Δ*ponA* cells 50 min after GlpQ incubation. (i) Phase contrast. (ii) Propidium iodide stain. Scale bars 5 m. **(E)** Same as (D) for wild-type cells (3,236 discrete tracks, four biological relicates). Inset: (i-ii) cell micrographs of (i) growing and (ii) non-growing cells, and (iii-iv)

480 kymographs of (iii) growing and (iv) non-growing cells, following the exit from GlpQ treatment. Scale
481 bars 5μm in (i,ii), 0.5μm in (iii,iv). Red dotted line in (iii) follows a processive Mbl filament. For positive
482 stain, see Fig. 2B ii. Scale bars 5µm. **(F)** Heatmap showing Δ*ponA* cell length growth rate $\lambda_l = \frac{1}{l}\frac{dl}{dt}$ when
483 exit from a 15-minute incubation with 10µM GlpQ was coupled to a 500mM hyperosmotic shock (3,036
484 discrete cell tracks, 3 biological replicates).

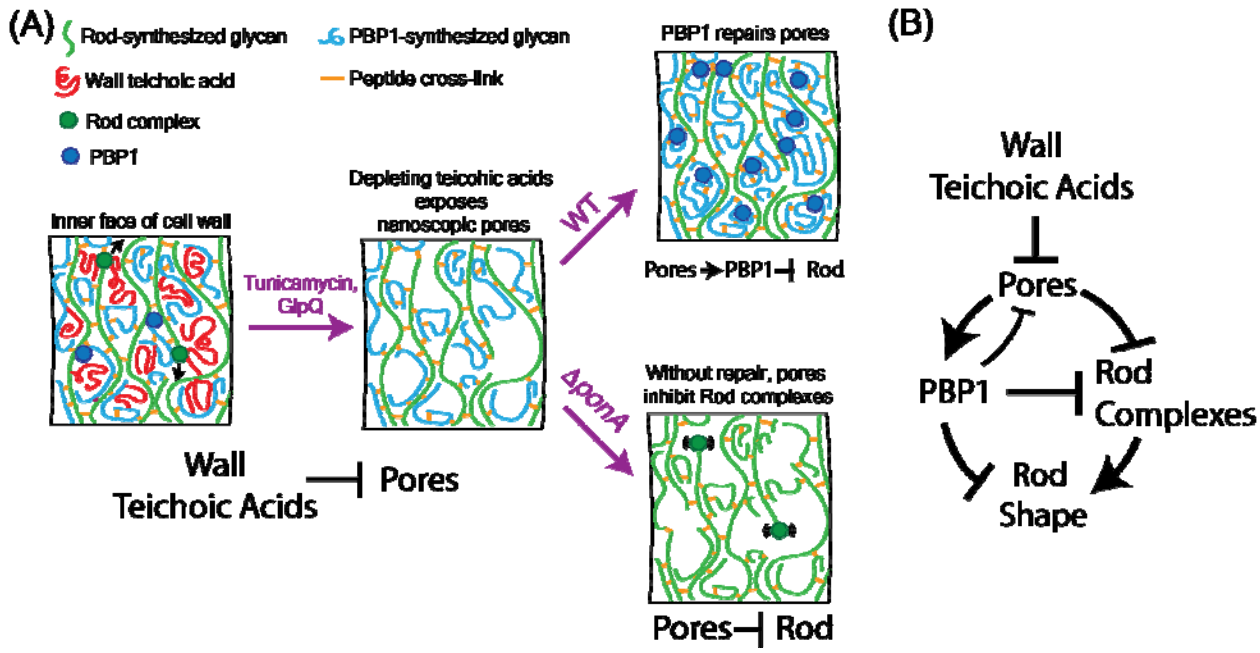

485

486 **Figure 4: (A)** Model illustration. During teichoic acid depletion of wild-type cells, denuded cell wall pores
487 are targeted by PBP1, competitively inhibiting Rod complexes and driving localized peptidoglycan
488 synthesis. This isotropic cell wall synthesis causes decreased growth and loss of cell shape. During
489 teichoic acid depletion of Δ*ponA* cells, denuded cell wall pores directly arrest Rod complex motion
490 through depletion of crosslinking acceptors. **(B)** Model.

491 **Methods**

492 **Microscopy**

493 All timelapse microscopy was performed with a Nikon Eclipse Ti2 microscope, outfitted with a
494 photometrics PRIME BSI CMOS camera and a Nikon 100X Plan Apo Phase Contrast objective, NA 1.45. All
495 non-TIRF fluorescence imaging used LED illumination. We conducted all imaging using CellASIC ONIX
496 microfluidic plates (Millipore B04A-03), using standard priming and media exchange protocols. We
497 heated all microscope stage components, CellASIC plates, and objectives to 37°C prior to imaging using a
498 microscope incubator outfitted with a heater. We performed our timelapse phase microscopy using 20s
499 timesteps, monitoring medium exchange using the dye AlexaFluor 647 at a final media concentration of
500 2.5µg/mL, with CY5 illumination adjusted to avoid any confounding effects of phototoxicity.

501 **TIRF Microscopy**

502 All TIRF microscopy was performed with the same Nikon Eclipse Ti2 microscope, using a COHERENT
503 488nm laser and 100X Plan Apo objective, NA 1.45, with 2s timesteps. We adjusted our laser power,
504 exposure time and TIRF alignment to minimize photobleaching, and used a fresh field of view for each
505 new timepoint to avoid any confounding effects of phototoxicity.

506 **Cell culture and transformation**

507 All cell culture was performed in LB media. All *in vivo* imaging and spot-assay experiments were
508 performed with log-phase cultures of OD600≤0.2. Transformations were performed in MC Media +
509 20mM $MgSO_4$. All cells were congenic with a PY79 strain background. Strains are tabulated in Sheet S1.

510 **Protein purification and application**

511 Protein was purified according to prior methods[1]. We incubated cell cultures of 500mL LB + 100 ug/mL
512 Ampicillin and 35 ug/mL Chloramphenicol at 37°C with shaking until they reached an OD600 of 0.6-0.8.

513 We shifted these cultures to 16°C, added IPTG (Isopropyl ß-D-1-thiogalactopyranoside) to a final
514 concentration of 0.5mM, and incubated with shaking for 18h. We centrifuged these cultures at 4°C,
515 resuspended in Buffer A (50 mM Tris-HCl + 200 mM NaCl + 1 mM CaCl2 + 1 mM MgCl2, pH 8.0) +
516 +25mM Imidazole and lysed by disruption in an Emulsiflex-C5. After disruption, we incubated the
517 supernatant with a column containing HisPur Ni-NTA Resin (ThermoFisher 88221), ran this column over
518 an Imidazole gradient, and visualized samples via SDS-PAGE with stain-free labeling (BioRad 1610183).
519 We pooled column elutions containing high protein concentrations, performed dialysis at 4°C overnight
520 in Buffer A, concentrated our samples with Amicon Ultra Centrifugal Filters (10KDa molecular weight
521 cutoff), and flash-froze single-use aliquots with liquid Nitrogen for storage at -80°C. We calculated our
522 protein concentration by nanodrop.

523 The Gram-positive cell wall imposes a substantial diffusion barrier to molecules above 15kDa (Akbary et
524 al., *in submission*). At 30.1kDa, GlpQ exceeds this limit substantially, rendering it necessary to partially
525 degrade the cell wall to allow GlpQ access to its target substrates. As such, we performed all GlpQ
526 incubations in PBS lacking divalent cations, to induce autolysis.

527 ***In vivo* bocillin labeling**

528 We grew cell cultures to early log-phase, back diluted into prewarmed LB to create multiple identical,
529 log-phase samples, and added tunicamycin (MP Biomedical 0215002805 and Cell Signaling Technology
530 12819) to each sample at successive time intervals of 10 min, to a final concentration of 0.5µg/mL. Prior
531 to lysis, we treated all cultures with Bocillin-FL (Invitrogen, B13233) simultaneously to a final
532 concentration of 1µg/mL, incubated for 2 min, then pelleted cells for cell lysate extraction. We treated
533 cell pellets with lysis buffer (20mM Tris pH 7.5, 1mM EDTA, 10mM $MgCl_2$, 1mg/mL Lysozyme, 1mM
534 PMSF, 10ug/mL DNAse I, 100ug/mL RNAse A). We added fresh Lysozyme, PMSF, DNAse I and RNAse A to

535 a lysis buffer stock for each preparation. We then visualized cell lysates via SDS-PAGE (FastCast 10%
536 Acrylamide, Bio-Rad 1610183) using a Cytiva Amersham Typhoon fluorescent imager.

537 **Wall teichoic acid measurement by flow cytometry**

538 We grew cell cultures to log-phase (OD600=0.1-0.2), then took two samples from a single cell culture,
539 washed 1X in PBS, and incubated in PBS + 40µM GlpQ or PBS + the equivalent volume of Buffer A for 15
540 min with rocking at 37°C. We then washed cells again 1X in PBS, and resuspended cells in PBS
541 supplemented with 200ug/mL of Concanavalin A-AlexaFluor 647 (Invitrogen, C21421) for 10min at 37°C,
542 with rocking. Concanavalin A is a lectin that binds glycosylation modifications along the teichoic acid
543 polymer[2,3]. We then washed cells again 1X in PBS, then resuspended samples in PBS for flow cytometry.
544 We performed our flow cytometry measurements with a Cytek Aurora set to 10,000 events per sample,
545 with gains adjusted to capture the full dynamic range of our population measurements. We consistently
546 calibrated the instrument to a low background (<10 events/second), and vigorously vortexed each
547 sample prior to acquisition. Since we were interested in statistics of the whole cell population, we
548 performed minimal gating (Fig. S6B). Since GlpQ preferentially cleaves non-glycosylated teichoic acids[1],
549 the GlpQ-mediated reduction in Concanavalin A staining for wild-type cells is likely an underestimate of
550 GlpQ-mediated teichoic acid cleavage. We used Δ*tagE* mutants to control for non-specific wheat-germ
551 agglutinin labeling, since TagE is responsible for teichoic acid glycosylation[4].

552 **Image Analysis and Tracking**

553 Cell tracking was performed using custom scripts written in ImageJ, MATLAB and Python. Our timelapse
554 image analysis pipeline involved the following steps: image alignment, background removal, and cell
555 tracking based on phase contrast images. Our single timepoint FDAA image analysis pipeline only
556 required background removal and cell segmentation based on phase contrast images, before calculating

557 cellular fluorescence based on background-corrected fluorescence images. All scripts are available for
558 download at: *https://github.com/felixbarber/WTA_Rod_complex_2024*.

559 **MreB filament tracking**

560 We detected and tracked our MreB and MbI filaments using custom Python scripts written by FB. For
561 filament detection, we used the "blob_log" function within scikit-image's "measure" module, selecting a
562 dynamical threshold throughout each TIRF timecourse to correct for partial photobleaching.

563 **Cell lysis tracking**

564 We tracked cell lysis by perfusing cells with propidium iodide at a final concentration of 2µg/mL, imaging
565 every 5 min with 100ms RFP at 10% power. Due to a high level of background signal following cell lysis,
566 we annotated cell lysis events semi-automated custom ImageJ macros.

567 **Analysis of peptidoglycan composition**

568 Peptidoglycan was prepared from cell lysates, digested with cellosyl (gift from Hoechst, Germany), and
569 the resulting muropeptides were reduced with sodium borohydride and analyzed by high-performance
570 liquid chromatography as previously described[5].

571 **Permeability Assays**

572 Cells were grown to log-phase and diluted 20-fold into a pre-warmed medium within the loading well of
573 a pre-heated CellASIC B04A microfluidic flow cell. The cells incubated for an additional 30 minutes prior
574 to loading into the imaging chamber. While imaging, fresh medium was perfused through the flow cell.
575 The cell-trapping mechanism used by the microfluidic chips had no detrimental effect on the elongation
576 of morphology of cell chains, as compared with cells growing on agarose pads or liquid culture[6].

577 To perform membrane lysis, the medium in the flow cell was exchanged with media + 5% N-
578 lauroylsarcosine (Sigma Aldrich L9150) for two minutes. We monitored detergent exchange using the
579 dye AlexaFluor 647 at a final media concentration of 5 µg/mL and imaged with 50 ms CY5 illumination at
580 10% intensity. After membrane lysis, the detergent in the flow cell was exchanged for media to wash the
581 cells.

582 For cells expressing mNeonGreen, we imaged every minute or every 5 minutes with 50 ms GFP at 100%
583 power. For cells expressing a tetracysteine-tagged ubiquitin, we imaged every minute with 50 ms GFP at
584 10% power. To label the tetracysteine-tagged ubiquitin, we incubated cells with 1 µM FlAsH-EDT_2 (4',5'-
585 bis(1,3,2-dithiarsolan-2-yl)-3',6'-dihydroxy-spiro[isobenzofuran-1(3H),9'-[9H]xanthen]-3-one; Cayman
586 Chemical 20704) for one hour prior to diluting the cells into the loading well, which also had 1 µM FlAsH-
587 EDT_2 in the medium.

588 Cell tracking and fluorescence quantification was performed using custom scripts written in MATLAB.

589 **Data Availability**

590 All datasets presented herein will be made publicly available.

591 **Code Availability**

592 All code used herein will be made publicly available at https://github.com/felixbarber.

Methods References

1. Myers, C. L. *et al.* Identification of Two Phosphate Starvation-induced Wall Teichoic Acid Hydrolases Provides First Insights into the Degradative Pathway of a Key Bacterial Cell Wall Component*. *Journal of Biological Chemistry* **291**, 26066–26082 (2016).
2. Koyano, Y., Okajima, K., Mihara, M. & Yamamoto, H. Visualization of Wall Teichoic Acid Decoration in Bacillus subtilis. *Journal of Bacteriology* **0**, e00066-23 (2023).
3. Lang, W. K. & Archibald, A. R. Relation between wall teichoic acid content and Concanavalin A binding in Bacillus subtilis 168. *FEMS Microbiology Letters* **20**, 163–166 (1983).
4. Allison, S. E., D'Elia, M. A., Arar, S., Monteiro, M. A. & Brown, E. D. Studies of the genetics, function, and kinetic mechanism of TagE, the wall teichoic acid glycosyltransferase in Bacillus subtilis 168. *J Biol Chem* **286**, 23708–23716 (2011).
5. Sassine, J., Sousa, J., Lalk, M., Daniel, R. A. & Vollmer, W. Cell morphology maintenance in Bacillus subtilis through balanced peptidoglycan synthesis and hydrolysis. *Scientific Reports* **10**, 17910 (2020).
6. Rojas, E. R., Huang, K. C. & Theriot, J. A. Homeostatic Cell Growth Is Accomplished Mechanically through Membrane Tension Inhibition of Cell-Wall Synthesis. *Cell Systems* **5**, 578-590.e6 (2017).

611 **Acknowledgements**

612 We thank Dr. Daniela Vollmer for preparation of peptidoglycan. ERR and FB were supported by NSF-
613 CAREER grant 2047404. WV received funding from the UK Biotechnology and Biological Sciences
614 Research Council (BBSRC) (BB/W013630/1). ZA was supported by NIH grant R35GM143057.

615 **Author Contributions**

616 FB, ZA, ZY, JB and LPL performed the experiments. FB, ZA, ZY, JB and LPL analyzed the data. FB and ER
617 wrote the manuscript.

618 **Declaration of Interests**

619 The authors declare no competing interests.

620 **Extended Data: Tables**

621 **Table S1:** List of strains used in this study.

Strain ID	Genotype/Plasmid	Figures used in this study	Source
bGL01	WT	1B,D, 2A-C, 2E-F, 3E, S1, S2A, S4, S5A, S6, S7C, S9A.	Gift from Garner Lab
bMD122	ΔmbI::sfGFP-mbI spec	1C, 3E inset, S3A-C, S8, Videos S2-S11.	Gift from Garner Lab
bEG291	ΔtagO::erm, ycgO::PxylA-tagO cat	S2B-C, S4A	Gift from Garner Lab
bYS009	mreB-40aa-mNeonGreen	S3D-F	Gift from Garner Lab
bMD599	ΔponA::kan	1D,2A-D, 3D, 3F, S5A, S9C-D	Gift from Garner Lab
bFB071	ΔtagO::erm	S1, S4B-C, S6	Gift from Garner Lab
bFB012	ΔmbI::sfGFP-mbI spec, ΔtagO::erm, ΔycgO::PxylA-tagO	S3G-I	This study
bFB079	ΔdacA::kan	1D	This study
bFB155	ΔtagE::erm	S6	This study
bFB145	ΔponA::PonA S390A kan	2A inset, 2C, S5A	This study
bFB149	ΔponA::PonA kan	Video S1	This study
bFB215	ΔtagO::erm, ΔycgO::PxylA-tagO cat ΔponA::kan	2B, S5B	This study
bFB262	ΔtagO::erm, ΔycgO::PxylA-tagO cat, ΔpbpD::kan	S5B	This study
bFB264	ΔtagO::erm, ΔycgO::PxylA-tagO cat, ΔponA::PonA S390A kan	S5B	This study

622

623 **Table S2:** List of primers used in this study.

Name	Sequence
oFB053	CTATACGAATAGCTTAGACAGC
oFB054	TAACAAGACGAACTCCAATTC
oFB055	GCGAACAATCAAGATAGGG
oFB056	TCGATCAATGCAATGTCTG
oFB094	TACAGCTCGATAATCTTTTCAG
oFB095	TTTGAACGGCATGATGG
oFB116	CGATAAAACCTCCTGTTAAAAC
oFB131	CAGAATTTCCGGTGTTCC
oFB132	CCTGATCACCAAGTATTTGAT
oFB133	GACGTTTTACGACAAGACC
oFB134	CAAAATCAACCCGTCAACTT
oFB148	AGGTGACAATCGTGTTAAAT
oFB149	CTCAGTTTCCGCTACATTG
oFB154	AAATTAAACAAAAAAGCCGTCACCTTTGGGGTGATGGCTTTTTTGTTCTGCTCCCTCGCT
oFB155	ATCACCCCAAAGGTGACGGCTTTTTTGTTTAATTTGTTTTTTCAATGGATGATGAGTTTG
oFB156	CTCAAACTAAGGCACAGCCTGGTGCGACCATAAAACCGATTTTGGACTACGGACCAGTTA
oFB157	CCAAAATCGGTTTTATGGTCGCACCAGGCTGTGCCTTAGTTTGAGTAGCATAGTTAAAGC
oFB159	TGGACTACGGACCAGTTA
oFB164	CTCAGAAGCTTTCTGATGG
oFB166	GATGCGGTATACCTTCTCAA
oFB173	AAGACTCAGGATGATACACA

oFB245	CGTATGGCAATGGGTCTTG
oFB246	GTTCATATTTATCAAGCTTTATAATAGCATAATGGCTA
oTY001	CACCGTACAGAAATATGCG
oTY002	ATATATTCGTAAATCGCTCTCG
oTY003	CGGAATCCATAATGGAAGC
oTY004	AACATAACCGTCTGAATAACC
oTY038	GATTCATCCCGACATCTCT
oTY039	GTAAGCTAGCCATTTCAGC

624

625 **Extended Data: Figures**

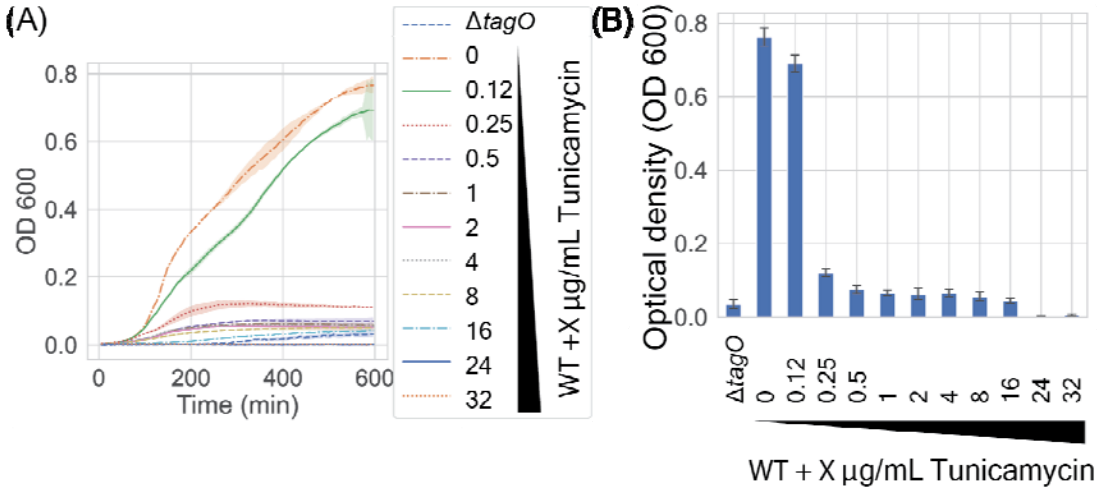

626

627 **Figure S1:** Low tunicamycin concentrations inhibit growth to precisely the same extent as deletion of
628 *tagO*. **(A)** Growth curves of cells grown with increasing tunicamycin concentrations in bulk culture. **(B)**
629 Saturating culture density plotted for data from (A). Representative data from one of three biological
630 replicates, with 4 technical replicates per condition. Complete growth arrest consistently occurs at
631 either 16 g/mL or 24 g/mL tunicamycin.

632

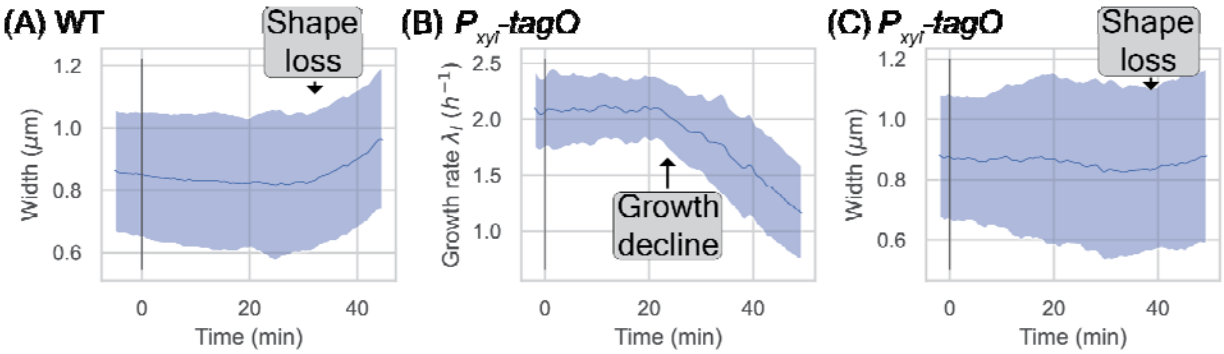

633

634 **Figure S2: (A)** Cell width of wild-type cells during 0.5 g/mL tunicamycin timecourse. Solid line shows
635 smoothed population median, error bars show standard deviation. Black line shows onset of
636 tunicamycin treatment. Increase in width corresponds to gradual loss of cell shape. Analysis performed
637 over 3,737 discrete cell tracks from 3 biological replicates. **(B-C)** Cell properties during growth response
638 of P_{xylA}-*tagO* cells to xylose depletion. **(B)** Cell length growth rate. Analysis performed over 1,217 discrete
639 cell tracks from 3 biological replicates. **(C)** Cell width. Analysis performed over 1,846 discrete cell tracks
640 from 3 biological replicates. Solid lines show smoothed population medians, error bars show standard
641 deviations. Black lines show onset of xylose depletion.

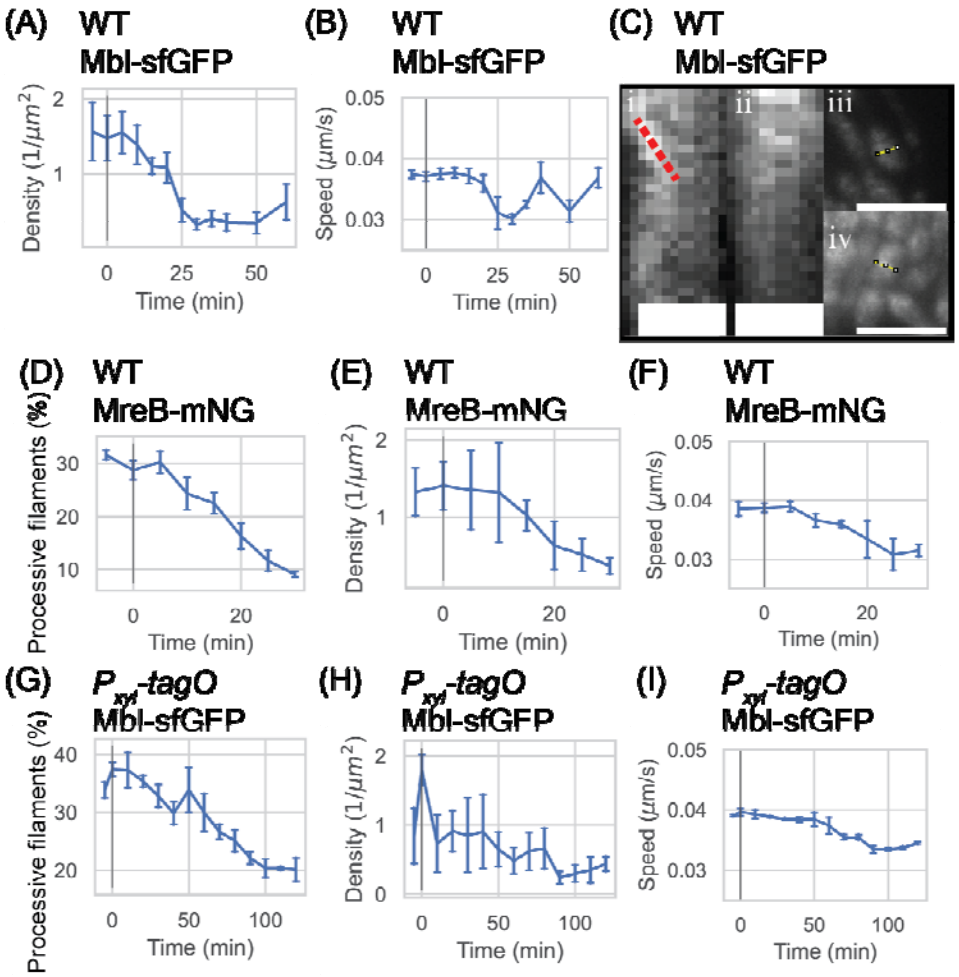

Figure S3: (A-B) Mbl-sfGFP activity time course for wild-type cells during 0.5 g/mL tunicamycin treatment. Analysis performed on 62,901 discrete filament tracks from 4 biological replicates. **(A)** Spatial density of processive filaments. **(B)** Average speed of processive filaments. **(C)** (i-ii) Representative kymographs from TIRF imaging of Mbl-sfGFP cells after 60 min tunicamycin treatment. Red dotted line follows a processive Mbl filament. Scale bars 1 m. (iii-iv) TIRF micrographs showing whole cells during a single timepoint of the kymographs in (i-ii) respectively. Yellow lines show kymograph traces. Scalebars 5 m. **(D-F)** MreB-mNeonGreen activity time course for wild-type cells during 0.5 g/mL tunicamycin treatment. Analysis performed on 30,805 discrete filament tracks from 3 biological replicates. **(D)** Percentage of processive filaments. **(E)** Spatial density of processive filaments. **(F)** Average speed of processive filaments. **(G-I)** Mbl-sfGFP activity time course of of P_{xylA}-*tagO* cells during xylose depletion. Analysis performed on 55,542 discrete filament tracks from 3 biological replicates. **(G)** Percentage of processive filaments. **(H)** Spatial density of processive filaments. **(I)** Average speed of processive

655 filaments. All error bars show 95% confidence intervals across biological replicates based on bootstrap
656 analysis.

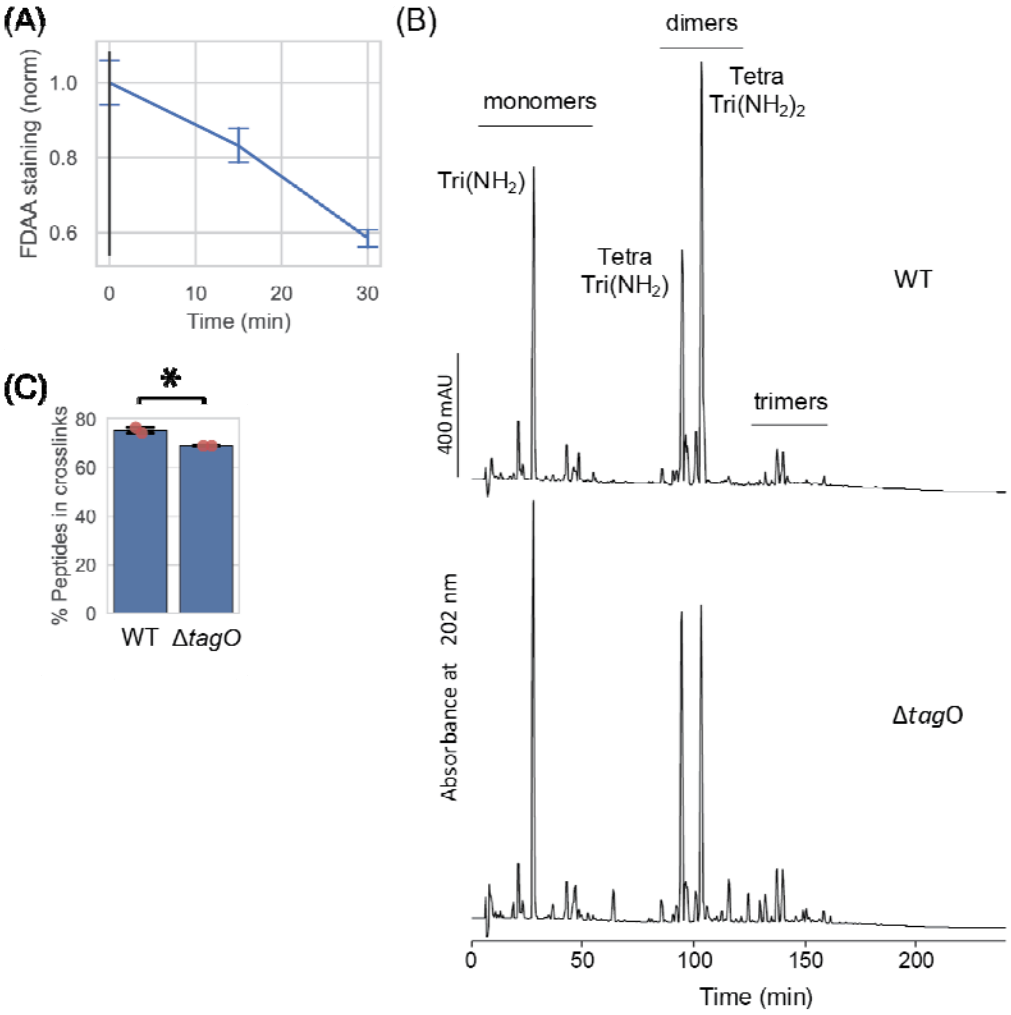

657

658 **Figure S4: (A)** Normalized mean cell envelope HADA staining for P_{xylA}-*TagO* cells during xylose depletion.
659 Black line shows xylose washout. Error bars show 95% confidence intervals. Analysis performed over 198
660 segmentations from 1 biological replicate. **(B)** High-performance liquid chromatograms of reduced
661 muropeptide samples isolated from wild-type and Δ*tagO* cells. Elution regions of the uncross-linked
662 monomers and cross-linked dimers and trimers are shown, and the three main muropeptides are
663 labelled. Tri(NH_2), GlcNAc-MurNAc(red)-L-Ala-D-iGlu-mDap (1 amidation); TetraTri(NH2), GlcNAc-
664 MurNAc(red)-L-Ala-D-iGlu-mDap-D-Ala-mDap-D-iGlu-L-Ala-(GlcNAc)MurNAc(red) (1 amidation);
665 TetraTri(NH2)2, GlcNAc-MurNAc(red)-L-Ala-D-iGlu-mDap-D-Ala-mDap-D-iGlu-L-Ala-
666 (GlcNAc)MurNAc(red) (2 amidations). GlcNAc, N-acetylglucosamine; MurNAc(red), N-acetylmuramitol; L-
667 Ala, L-alanine; D-iGlu, D-isoglutamic acid; mDap, meso-diaminopimelic acid; D-Ala, D-alanine. **(C)**

668 Percentage of peptide stems in peptidoglycan crosslinks as measured within cell walls purified from
669 wild-type and Δ*tagO* cells by HPLC. Two biological replicates per strain. Mean values calculated across
670 biological replicates. Error bars show 95% confidence intervals. Individual datapoints shown in red.
671 Statistical significance calculated using Student's T-test, $P<0.05$.

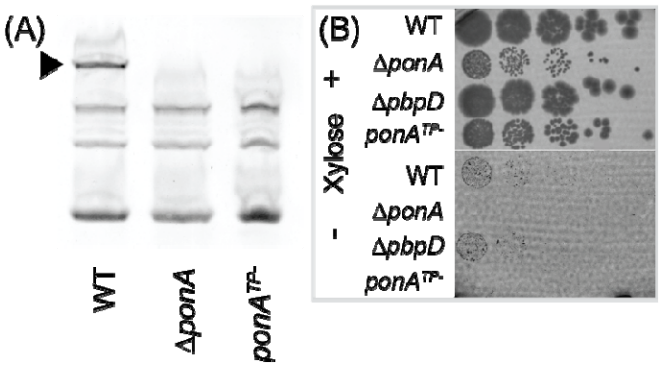

Figure S5: (A) SDS-PAGE on whole cell lysates from cells incubated with fluorescently conjugated β-lactam, bocillin. Black arrow shows PBP1, which is present in wild-type but absent in *ΔponA* and not labeled in $ponA_{S390A}$ cell lysates. **(B)** Spot assays for P_{xylA}-*tagO*, *ponA* mutant strains grown in the presence and absence of *tagO* induction with 30mM xylose.

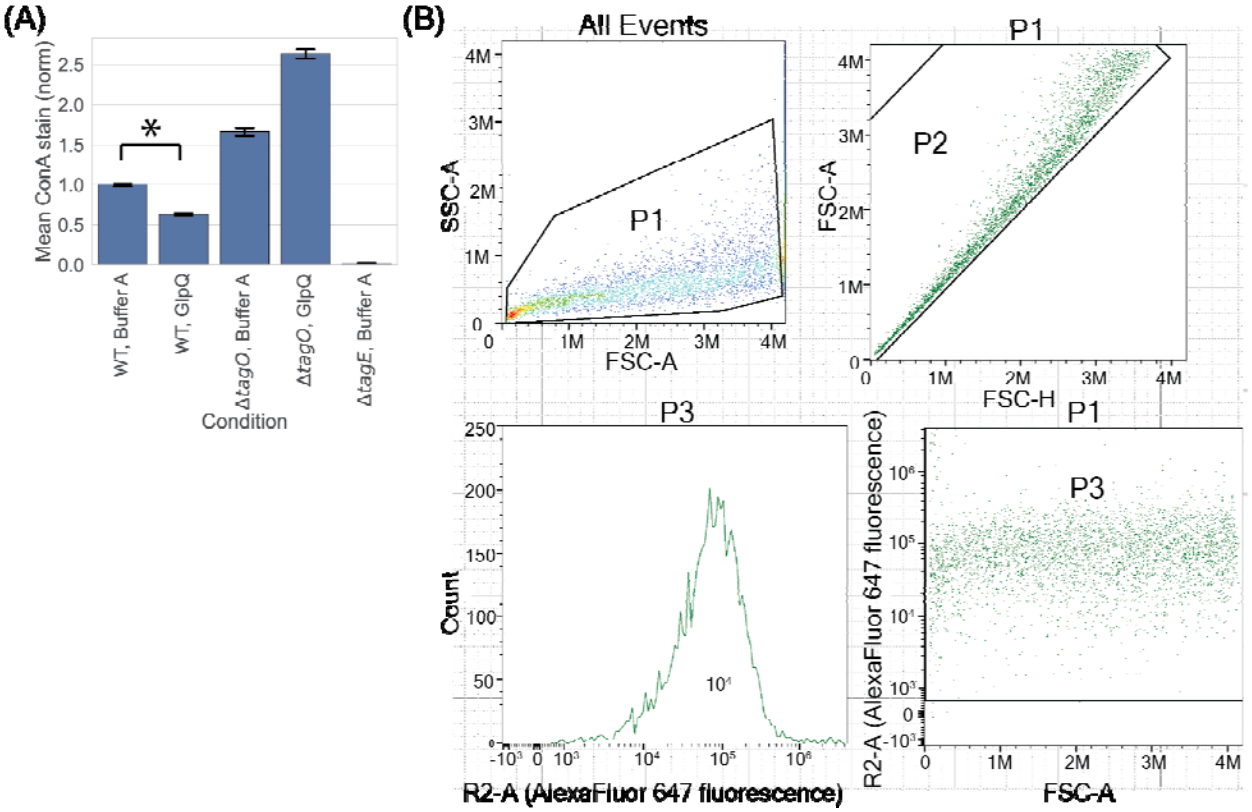

Figure S6: (A) Mean fluorescence intensity of Concananvalin A-AlexaFluor647 cell staining, following incubation either with PBS + Buffer A, or with PBS + GlpQ, measured by flow cytometry. GlpQ-treated cells show decreased Concanavalin A staining relative to PBS-treated cells (Welch's T-test, P value < 10^{-3}), consistent with GlpQ enzymatically cleaving teichoic acids from the cell wall. Δ*tagO* cells show no such decrease in Concanavalin A staining upon GlpQ incubation, and Δ*tagE* cells lacking the enzyme responsible for teichoic acid glycosylation show negligible labeling. We observed increased Concanavalin A-staining in Δ*tagO* cells relative to wild-type that was amplified during GlpQ treatment, possibly due to the clumping phenotype of this mutant. Error bars show 95% confidence intervals across 3 biological replicates, 10,000 samples per replicate. **(B)** Example of flow cytometry gating process used to generate data in (A).

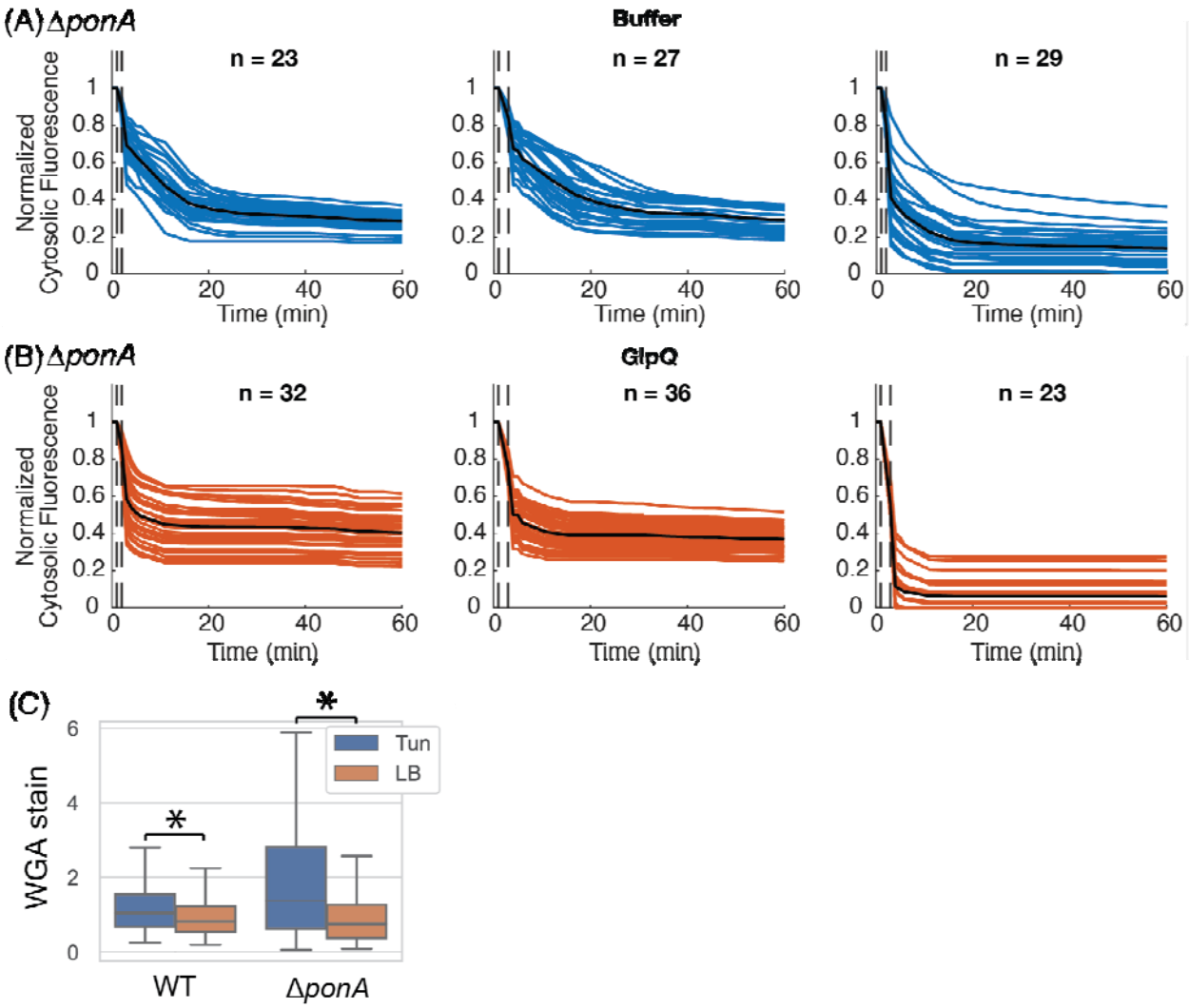

688

689 **Figure S7:** Ubiquitin-FlAsH immediately leaves the cytosol upon wall teichoic acid digestion and
690 simultaneous lysis in Δ*ponA* cells. **(A-B)** Individual Ubiquitin-FlAsH fluorescent traces and experimental
691 replicates following 2 min incubation with PBS +5% N-lauroylsarcosine and either **(A)** Buffer A alone, or
692 **(B)** 40uM GlpQ. Cell counts are shown in figure captions. **(C)** Fluorescence of cells labeled with a wheat-
693 germ agglutinin-AlexaFluor488 conjugate after incubation with LB alone or LB supplemented with
694 tunicamycin for either 10 min (wild-type) or 20 min (Δ*ponA*). Wild-type LB: 247 cells. Wild-type
695 tunicamycin: 148 cells. Δ*ponA* LB: 197 cells. Δ*ponA* tunicamycin: 136 cells. 3 biological replicates per
696 condition.

697

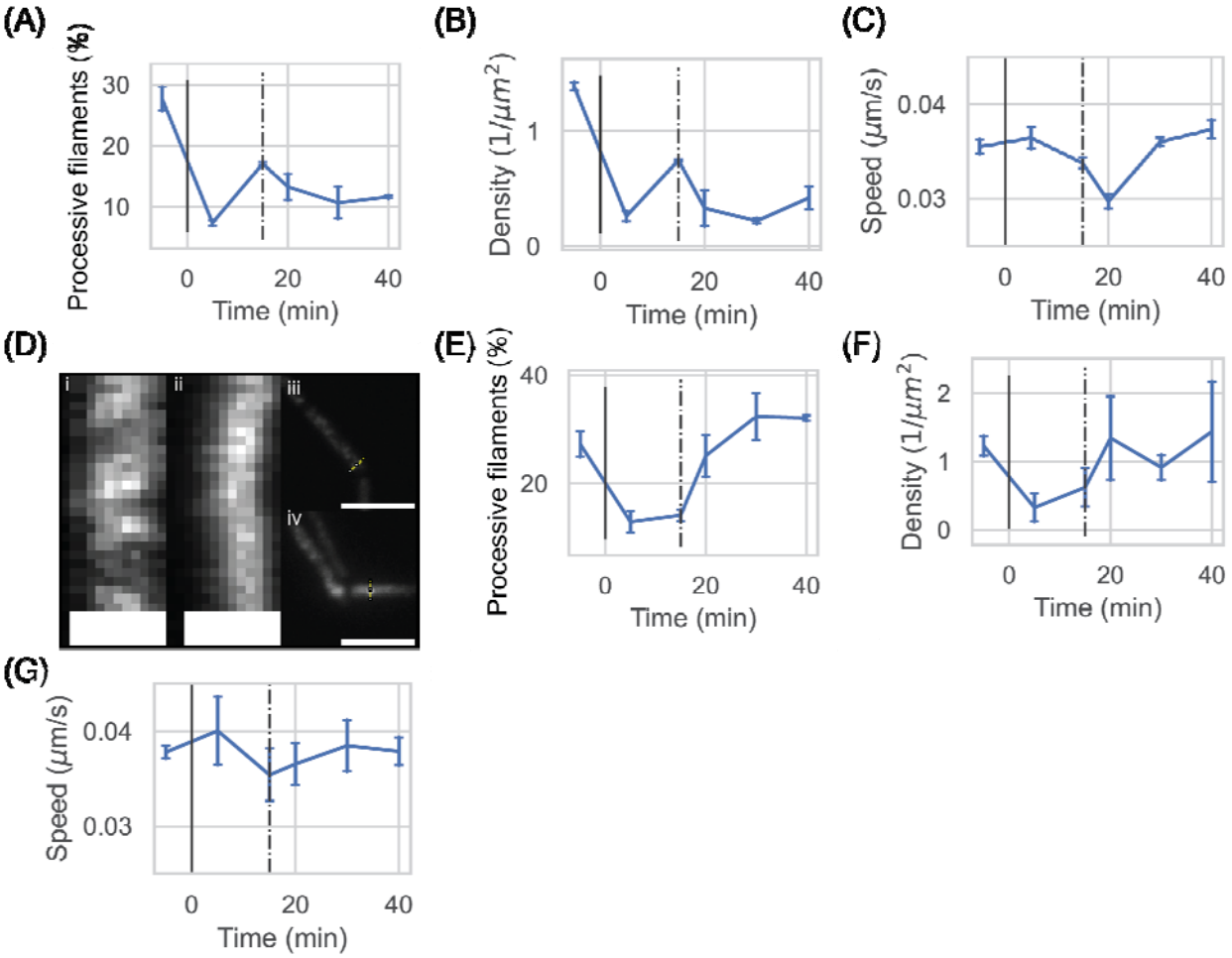

698

699 **Figure S8: (A-C)** Mbl-sfGFP activity time course during 25 M GlpQ treatment. Analysis performed on
700 10,976 discrete filament tracks from 2 biological replicates. **(A)** Percentage of processive filaments. **(B)**
701 Spatial density of processive Mbl-sfGFP filaments. **(C)** Speed of processive Mbl-sfGFP filaments. All error
702 bars show 95% confidence intervals across biological replicates based on bootstrap analysis. **(D)**
703 Representative kymographs from TIRF imaging of (i) growing and (ii) non-growing wild-type cells 35 min
704 after release from GlpQ treatment. Scalebars 1 m. (iii-iv) TIRF micrographs showing whole cells during a
705 single timepoint of kymographs in (i-ii) respectively. Yellow lines show kymograph traces. Scalebars 5 m.
706 **(E-G)** Mbl-sfGFP and MreB-mNeonGreen activity time course during PBS treatment. Analysis performed
707 on 11,150 discrete filament tracks from 3 independent experiments. Data pooled from experiments with
708 15min and 20min PBS treatment. **(E)** Percentage of processive filaments. **(F)** Spatial density of processive
709 Mbl-sfGFP filaments. **(G)** Speed of processive filaments.

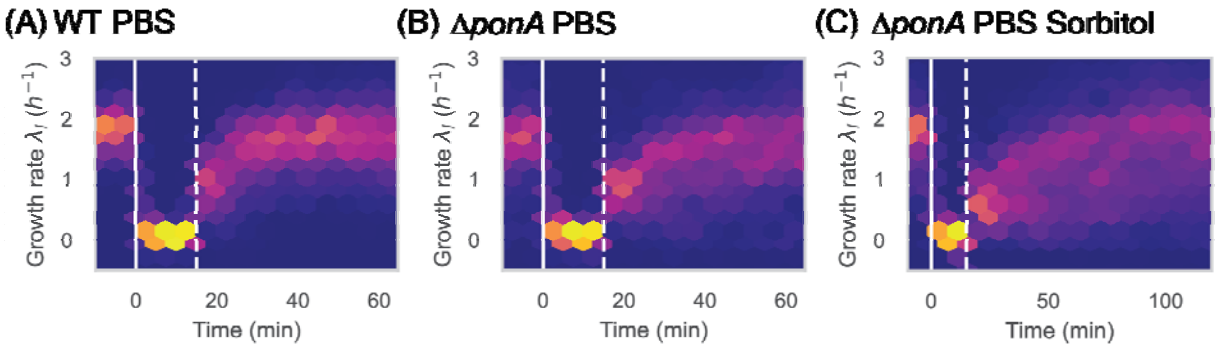

Figure S9: (A-B) Heat maps showing growth rate −— during recovery after incubation with either PBS + denatured GlpQ or GlpQ buffer for 15 min. **(A)** wild-type cells (3,830 discrete tracks, two independent experiments with denatured GlpQ, one with equivalent volume GlpQ buffer, no differences between conditions observed). **(B)** Δ*ponA* cells (2,142 discrete cell tracks, 3 biological replicates). **(C)** Heatmap showing Δ*ponA* cell length growth rate −— following 15-minute incubation with PBS + GlpQ Buffer (7,097 discrete cell tracks, 3 biological replicates), where exit from incubation is coupled to a 500mM Sorbitol hyperosmotic shock. Solid line shows onset of PBS incubation, dotted line shows exit into LB + Sorbitol.

719 **Video S1:** 100X Phase timelapse of wild-type growth during 0.5 μg/mL tunicamycin treatment.
720 tunicamycin exposure starts at 5min. Scale bar 5μm.

721 **Video S2:** 100X TIRF imaging of Mbl-sfGFP motion in wild-type cells grown in LB. Scale bar 5μm.

722 **Video S3:** 100X TIRF imaging of Mbl-sfGFP motion in wild-type cells grown in LB. Scale bar 5μm.

723 **Video S4:** 100X TIRF imaging of Mbl-sfGFP motion in wild-type cells treated with 0.5 μg/mL tunicamycin
724 for 30min. Scale bar 5μm.

725 **Video S5:** 100X TIRF imaging of Mbl-sfGFP motion in wild-type cells treated with 0.5 μg/mL tunicamycin
726 for 30min. Scale bar 5μm.

727 **Video S6:** 100X TIRF imaging of Mbl-sfGFP motion in wild-type cells treated with 0.5 μg/mL tunicamycin
728 for 60min. Scale bar 5μm.

729 **Video S7:** 100X TIRF imaging of Mbl-sfGFP motion in wild-type cells treated with 0.5 μg/mL tunicamycin
730 for 60min. Scale bar 5μm.

731 **Video S8:** 100X TIRF imaging of Mbl-sfGFP motion in growing wild-type cells treated with 25uM GlpQ for
732 15 minutes. Timelapse taken 25 min post release into LB. Scale bar 5μm.

733 **Video S9:** 100X TIRF imaging of Mbl-sfGFP motion in growing wild-type cells treated with 25uM GlpQ for
734 15 minutes. Timelapse taken 35 min post release into LB. Scale bar 5μm.

735 **Video S10:** 100X TIRF imaging of Mbl-sfGFP in non-growing wild-type cells treated with 25uM GlpQ for
736 15 minutes. Timelapse taken 25 min post release into LB. Scale bar 5μm.

737 **Video S11:** 100X TIRF imaging of Mbl-sfGFP in non-growing wild-type cells treated with 25uM GlpQ for
738 15 minutes. Timelapse taken 35 min post release into LB. Scale bar 5μm.